Applied Catalysis B: Environmental 136–137 (2013) 308–316

Contents lists available at SciVerse ScienceDirect

Applied Catalysis B: Environmental

journal homepage: www.elsevier.com/locate/apcatb

$Co/Ce_xZr_{1-x}O_2$ solid-solution catalysts with cubic fluorite structure for carbon dioxide reforming of methane

Shanghong Zeng, Xiaohong Zhang, Xiaojuan Fu, Lei Zhang, Haiquan Su*, Hui Pan

Inner Mongolia Key Laboratory of Chemistry and Physics of Rare Earth Materials, School of Chemistry and Chemical Engineering, Inner Mongolia University, Hohhot 010021, China

ARTICLE INFO

Article history:
Received 29 April 2012
Received in revised form 7 January 2013
Accepted 12 February 2013
Available online 19 February 2013

Keywords:
$Ce_xZr_{1-x}O_2$
Cobalt catalyst
Carbon deposition
CH_4/CO_2 reforming

ABSTRACT

The $Co/Ce_xZr_{1-x}O_2$ catalysts were prepared by the impregnation method and characterized via BET, NH_3-TPD, XRD, H_2-TPD, H_2-TPR, TEM and TG–DSC techniques. The study showed that the Co_3O_4 crystallites had better dispersion on the cubic fluorite $Ce_xZr_{1-x}O_2$ supports compared with on the ZrO_2 and CeO_2, and the $Co/Ce_{0.6}Zr_{0.4}O_2$ retained the cubic fluorite structure after the reaction. The $Ce_{0.6}Zr_{0.4}O_2$ catalyst showed good catalytic performance, which was attributed to the alkalescence of support surface, better dispersion of active species, better textural property and reducibility. The deposition carbon over the $Co/Ce_{0.6}Zr_{0.4}O_2$ catalyst mainly existed in the form of low-temperature carbon.

1. Introduction

In recent years there has been a considerable interest in investigating the CO_2 reforming of methane to syngas ($CH_4 + CO_2 \rightarrow 2CO + 2H_2$) process, which is environmentally friendly as it consumes two greenhouse gasses [1–5]. The low H_2/CO ratio is preferentially used for the production of liquid hydrocarbons in the Fischer–Tropsch synthesis and for the production of formaldehyde and polycarbonate [5,6]. However, this catalytic process has two main problems: the reaction temperature as high as 800 °C is required for CH_4 and CO_2 high conversion, and the catalyst is easily deactivated due to carbon deposition during the reaction [7–9]. Carbon originates mainly from two reactions: CH_4 decomposition ($CH_4 \rightarrow C + 2H_2$) and CO disproportionation ($2CO \rightarrow C + CO_2$). CH_4 decomposition is an endothermic reaction and CO disproportionation is an exothermic reaction, thus methane dehydrogenation is the main reason for carbon deposition at high temperature.

The noble metals, such as Pt, Pd, Rh and Ru, have shown to be active and selective in carbon dioxide reforming of methane by minimizing coke formation. However, the low availability and high cost of noble metals make them unfeasible for industrial scale operations [1,3,6,10,11]. The supported Ni catalysts are commonly studied because of their low cost, but nickel easily induces carbon deposition [4,5,9,12]. In the previous research, the addition of cobalt into nickel-based catalysts resulted in a large decrease of the carbon formation because of high metal dispersion and strong metal–support interaction [4]. Therefore, the cobalt catalysts have been a new focus of attention and reveal considerable activity for the CH_4/CO_2 reaction, which suggests that cobalt might be a suitable metal for this catalytic process [7,8,13].

Anderson and Boudart [14] mentioned that the dispersion of some metals is proportional to the Lewis acidity of support surface. They thought that it is possible that the metallic atoms easily disperse on the Lewis acid sites [14]. Therefore, the catalysts can provide more active sites for CH_4 activation when the supports possess stronger acidity. However, the acidity of supports reduces CO_2 adsorption and activation ability, resulting that the rate of CH_4 carbon deposition is greater than that of CO_2 carbon consumption. Masai et al. [15] studied the relationship between the acidity of support and catalytic performance over the Pd-based catalyst. The results showed that the acidic centers of γ-Al_2O_3 and $MgO–SiO_2$ can improve the dispersion of metallic Pd and enhance catalyst activity. Ji et al. [16] reported that the order of catalytic activity and anti-coke deposition is $Ni/Al_2O_3 > Ni/MgO > Ni/SiO_2$ for the Ni-based catalysts of different supports. The study suggested that the dispersion of active metal is main reason for influencing catalytic activity and carbon deposition over the Ni-based catalysts in CO_2/CH_4 reforming reaction [3–5,9,16]. In addition, the catalyst is difficult to reduce when the interaction becomes stronger between metal and support, but they show higher activity and stability due to the greater dispersion of metal after reduction.

The CO_2/CH_4 reforming is a high-temperature reaction, requiring the catalyst with a high thermal stability. $CeO_2–ZrO_2$ solid

* Corresponding author. Tel.: +86 471 4992979; fax: +86 471 4992979.
E-mail addresses: haiquansu@yahoo.com, haiquansu@sina.com (H. Su).

0926-3373/$ – see front matter © 2013 Elsevier B.V. All rights reserved.
http://dx.doi.org/10.1016/j.apcatb.2013.02.019

solution has attracted much attention due to its good oxygen storage capacity, thermal resistance and redox promotion property [17–23]. Noronha et al. [11] reported that the catalytic activity of Pt/ZrO_2 was greatly enhanced by the addition of Ce to the support. The activity went through a maximum at a composition $Pt/Ce_{0.5}Zr_{0.5}O_2$. Wang et al. [13] reported that the $Co\text{-}Ce_{0.8}Zr_{0.2}O_2$ catalyst possessed several advantages in CO_2/CH_4 reforming reaction. The charge effect of cubic $Ce_{0.8}Zr_{0.2}O_2$ with CoO_x species improved the sample reducibility. The catalyst with cubic phase had smaller nano-crystallite sizes of Co_3O_4 than the other catalysts with tetragonal and mixed phases. Therefore, the cubic $Co\text{-}Ce_{0.8}Zr_{0.2}O_2$ catalyst gave rise to lower apparent activation energy and exhibited a higher activity and stability in the CO_2/CH_4 reforming reaction.

In this work, we prepared the $Co/Ce_{0.6}Zr_{0.4}O_2$ and $Co/Ce_{0.33}Zr_{0.67}O_2$ catalysts with cubic fluorite structure in order to investigate the influence of acid–base property, synergy effect and structure on the catalytic performance of cobalt catalysts.

2. Experimental

2.1. Catalyst preparation

The $Ce_xZr_{1-x}O_2$ supports with two ratios of Ce/Zr were prepared by the hydrothermal method from the corresponding chemicals: $Ce(NO_3)_3{\cdot}6H_2O$ (99.9%, Alfa Aesar) and $ZrOCl_2{\cdot}8H_2O$ (99.9%, Alfa Aesar). The above chemicals were mixed into the aqueous solution, and then $NH_3.H_2O$ was added dropwise to the above solution until the pH value of the mixture was adjusted to approximate 10. The obtained solution was transferred into a stainless steel autoclave with 120 ml-capacity Teflon liner and heated for 60 h. The supports after centrifuging, washing and drying were calcined at 500 °C for 3 h in atmospheric pressure.

The supports were impregnated with $Co(NO_3)_3$ (99.9%, Alfa Aesar) solution for three times with equal volume impregnation. After impregnation, the samples were laid for 24 h, dried at 80 °C and calcined at 400 °C for 4 h in air atmosphere in order to get the $Co/Ce_xZr_{1-x}O_2$ catalysts. The above method also was used to prepare the Co/CeO_2 and Co/ZrO_2 catalysts. The loading content of cobalt was 10 wt.% in the above catalysts.

2.2. Catalyst characterization

2.2.1. NH_3-TPD analysis

The NH_3-TPD (temperature programmed desorption) technique was employed to determine the acidity of supports. They were conducted on Micromeritics ASAP2920 equipped with a thermal conductivity detector (TCD). Prior to the measurement, the supports were purged in flowing He at 500 °C for 2 h, and then cooled to 30 °C. The supports were treated with anhydrous NH_3 gas (5% NH_3 in He) until the outlet NH_3 concentration was stable. After removing physically adsorbed ammonia from the supports by flushing them with helium for 1 h, the supports were heated from 50 °C to 900 °C at a ramping rate of 10 °C/min.

2.2.2. X-ray diffraction (XRD)

The powder X-ray diffraction was performed on a MAC Science diffractometer. The diffraction patterns of the samples were recorded at room temperature with Cu Kα source (λ = 0.15406 nm) and a power setting of 40 kV and 100 mA in the range of 2θ between 10° and 80°.

2.2.3. Temperature programmed desorption (H_2-TPD)

The H_2-TPD measurements were carried on a Micromeritics ASAP2920 unit. At first, the catalysts were reduced at 450 °C for 12 h and cooled to 100 °C in flowing hydrogen, and the samples were purged at 100 °C for 1 h under an argon stream in order to remove the species of physical adsorption before increasing the temperature to 450 °C. Then the catalysts were held at 450 °C under flowing argon to desorb the remaining chemisorption hydrogen until the TCD signal returned to the baseline. The amount of desorbed hydrogen was calculated by comparing the integrated TPD spectrum with the mean areas of calibrated hydrogen pulses.

2.2.4. Temperature-programmed reduction (TPR)

The H_2-TPR experiments were conducted on a TP-5080 adsorption instrument. The samples were swept in nitrogen at 300 °C for 1 h and then cooled to room temperature. The reduction profiles were collected in the 5% H_2/N_2 gas mixture from room temperature to 900 °C. The flow rate of the gas was 40 ml/min and the heating rate was 10 °C/min. The water produced in the experiments was trapped with the molecular sieve.

2.2.5. N_2 adsorption–desorption isotherms

The textural properties of the samples were determined by nitrogen physisorption at liquid nitrogen temperature using a Micromeritics Apparatus (Model ASAP2020). The surface area and pore size distribution were determined by the Brunauer–Emmett–Teller (BET) and the Barrette–Joynere–Halenda (BJH) methods, respectively.

2.2.6. High resolution transmission electron microscopy (HRTEM)

The transmission electron microscopy images of the samples were performed via a JEOL 2010 transmission electron microscope. The sample was dispersed into ethanol with ultrasonic treatment for 10 min, and a drop of the suspension was placed on a copper grid for TEM observation.

2.2.7. Thermogravimetric and thermal analyses (TG–DSC)

The carbon deposition analyses of the spent catalysts were performed via a STA 409PC thermal analysis device in an air stream from room temperature to 900 °C with a heating rate of 10 °C/min.

2.3. Catalytic performance tests

The carbon dioxide reforming of methane was performed at atmospheric pressure in a stainless steel fixed-bed reactor with an inner diameter of 8.7 mm. The reactor temperature was measured via a thermocouple positioned at the middle of catalyst bed. The amount of catalyst used in the reaction was 0.05 g with the particle size in the range from 45 to 75 μm, and it was diluted with the quartz sand. Prior to conducting the catalytic reaction, the catalysts were reduced in situ using 10% H_2 in Ar stream at 650 °C for 1 h, and then fed with the reactant gas mixture of CH_4 (99.99%) and CO_2 (99.99%) at a GHSV of 8000 ml g_{cat}^{-1} h^{-1}. The mole ratio of CH_4 and CO_2 was 1:1 and the reaction temperature was controlled from 400 °C to 800 °C. The gas reactants and products were analyzed via a SP6890 gas chromatograph equipped with a TCD detector, and TDX-01 column was used to separate CO_2, CH_4, H_2, and CO.

The CH_4 and CO_2 conversion as well as H_2 and CO selectivity (all calculated in units of mol%) were defined as follows:

$$X_{CH_4}(\%) = \frac{F_{in} \times 50\% - F_{out} \times I_{CH_4}}{F_{in} \times 50\%}$$

$$X_{CO_2}(\%) = \frac{F_{in} \times 50\% - F_{out} \times I_{CO_2}}{F_{in} \times 50\%}$$

$$S_{H_2}(\%) = \frac{F_{out} \times I_{H_2}}{2 \times (F_{in} \times 50\% - F_{out} \times I_{CH_4})}$$

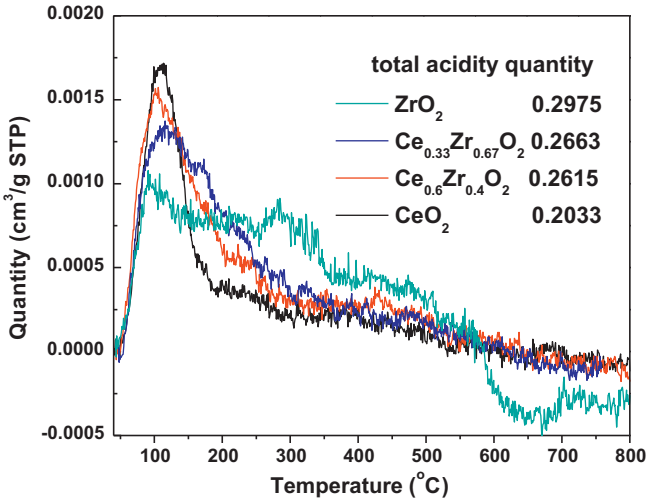

Fig. 1. NH_3-TPD profiles of the different supports.

$$S_{CO}(\%) = \frac{F_{out} \times I_{CO}}{(F_{in} \times 50\% - F_{out} \times I_{CH_4}) + (F_{in} \times 50\% - F_{out} \times I_{CO_2})}$$

where $F_{in/out}$ was the flow rate in the feed or effluent of total components, and I_i was the molar fraction of component in the gaseous feed or effluent.

3. Results and discussion

3.1. NH_3-TPD analysis

The NH_3-TPD measurements were performed in order to test the acidity of as-prepared supports. As shown in Fig. 1, the order of total acidity quantity was $ZrO_2 > Ce_{0.33}Zr_{0.67}O > Ce_{0.6}Zr_{0.4}O_2 > CeO_2$. It was evident that the addition of cerium reduced the acidity of support. The report [14] showed that the dispersion of some metals was proportional to Lewis acidity of support surface, and the possible reason was that the metal atoms easily dispersed on the Lewis acid sites.

Table 1
Lattice parameter and textural property of supports and catalysts.

Sample	Lattice parameter a(Å)[a]	BET Surface area (m^2/g)	Pore Volume (cm^3/g)	Pore Size (nm)
ZrO_2	–	44.60	0.28	25.07
$Ce_{0.33}Zr_{0.67}O_2$	5.239	90.97	0.32	13.88
$Ce_{0.6}Zr_{0.4}O_2$	5.304	89.54	0.28	12.73
CeO_2	5.406	83.30	0.24	10.12
Co/ZrO_2	–	40.76 (39.83)[b]	0.20	20.02
$Co/Ce_{0.33}Zr_{0.67}O_2$	5.329	81.89 (60.01)[b]	0.23	11.26
$Co/Ce_{0.6}Zr_{0.4}O_2$	5.361	73.58 (56.65)[b]	0.21	11.30
Co/CeO_2	5.404	33.45 (31.48)[b]	0.086	9.04

[a] Lattice parameter of cubic fluorite-type phase.
[b] BET surface area of the spent catalysts.

3.2. XRD measurements

Fig. 2 showed the XRD patterns of different supports. It could be seen that ZrO_2 existed in monoclinic and tetragonal phase mixture and CeO_2 was cubic fluorite structure. For CeO_2 support, the 2θ values of reflections appeared at 28.57°, 33.01°, 47.56°, 56.24°, 59.10°, 69.58° and 76.70°, respectively corresponding to (1 1 1), (2 0 0), (2 2 0), (3 1 1), (2 2 2), (4 0 0) and (3 3 1) planes of the cubic fluorite structure. Comparable to CeO_2, the reflection peaks were shifted to 29.78°, 34.43°, 49.58°, 58.66° and 72.33° for $Ce_{0.33}Zr_{0.67}O_2$ support, and to 28.97°, 33.36°, 48.15°, 57.11° and 70.26° for $Ce_{0.6}Zr_{0.4}O_2$ support, indicating that the smaller Zr^{4+} ions (0.084 nm) entered into the lattice of CeO_2 [13,18]. In general, Vegard's law was widely accepted to confirm the presence of solid solution. As showed in Table 1, the linear relationship of x and lattice parameters showed the formation of $Ce_xZr_{1-x}O_2$ solid solution in this work. It was evident that all the reflection peaks of solid solution were corresponding to the reflection peaks of cubic fluorite structure of CeO_2, suggesting that the $Ce_xZr_{1-x}O_2$ solid solution retained the cubic fluorite structure of CeO_2 support in despite of the low ratio of Ce to Zr.

Fig. 3 showed the XRD patterns of catalysts after calcination at 400 °C. The 2θ value of reflection at 36.95° corresponded to (3 1 1) plane of the Co_3O_4 spinel structure, indicating that Co_3O_4 was loaded on the supports. In addition, the reflection peaks of supports had no obvious change over the catalysts. The crystallite size was estimated by applying the Scherrer equation $d = k\lambda 180^\circ/(B\cos\theta\pi)$ to the more intense peaks of Co_3O_4, and the Co^0 particle size was calculated from the equation of $d(Co^0) = 0.75 \times d(Co_3O_4)$ [24]. Furthermore, the dispersion degree of cobalt ($D(Co_3O_4)$) was calculated by the formula of $D(Co_3O_4) = 96/d(Co^0)$ under the assumption

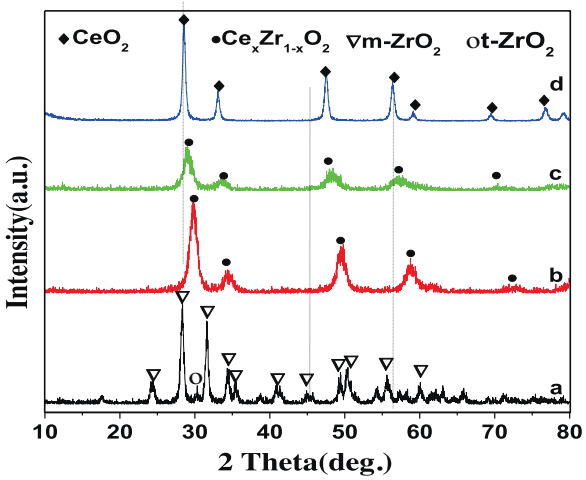

Fig. 2. XRD patterns of the different supports: (a) ZrO_2; (b)$Ce_{0.33}Zr_{0.67}O_2$; (c)$Ce_{0.6}Zr_{0.4}O_2$; (d) CeO_2.

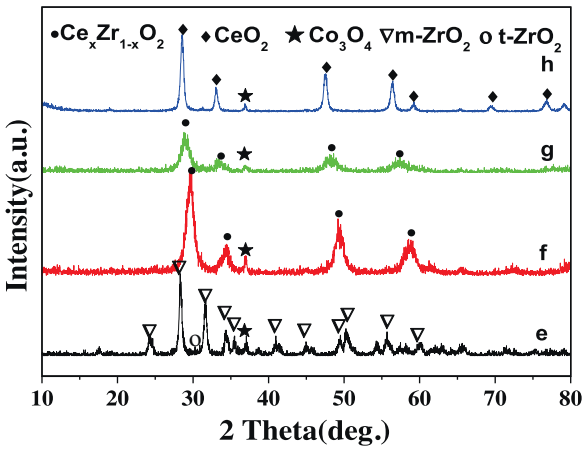

Fig. 3. XRD patterns of the catalysts: (e) Co/ZrO_2; (f) $Co/Ce_{0.33}Zr_{0.67}O_2$; (g) $Co/Ce_{0.6}Zr_{0.4}O_2$; (h) Co/CeO_2.

Table 2
Average crystallite size and dispersion degree of the catalysts.

Sample	Crystallite size (nm)		Dispersion degree (%) $D(Co_3O_4)$[c]	Metal dispersion (%) $D(Co_3O_4)$[d]
	$d(Co_3O_4)$[a]	$d(Co^0)$[b]		
Co/ZrO_2	26.1	19.6	3.7	9.3
$Co/Ce_{0.33}Zr_{0.67}O_2$	22.2	16.7	4.3	13.4
$Co/Ce_{0.6}Zr_{0.4}O_2$	26.0	19.5	3.7	13.0
Co/CeO_2	47.3	35.5	2.0	12.7

[a] Calculated from the Scherrer equation according to the (3 1 1) diffraction peak of Co_3O_4.
[b] Calculated from the equation of $d(Co^0) = 0.75 \times d(Co_3O_4)$.
[c] Calculated from the formula of $d(Co^0) = 96/D(Co_3O_4)$.
[d] Calculated from the H_2-TPD data.

that the particles of metallic cobalt were spherical and had uniform site density (14.6 atoms/nm^2) after reduction [24], which was also measured by H_2-TPD. As shown in Table 2, the Co_3O_4 crystallite size of $Co/Ce_{0.33}Zr_{0.67}O_2$ catalyst was the smallest and the dispersion degree of cobalt was the biggest. The order of dispersion degree was $Co/Ce_{0.33}Zr_{0.67}O_2 > Co/Ce_{0.6}Zr_{0.4}O_2 = Co/ZrO_2 > Co/CeO_2$ according to the formula as well as $Co/Ce_{0.33}Zr_{0.67}O_2 > Co/Ce_{0.6}Zr_{0.4}O_2 > Co/CeO_2 > Co/ZrO_2$ via the analysis of H_2-TPD, indicating a good dispersion of Co_3O_4 crystallites on the cubic fluorite $Ce_xZr_{1-x}O_2$ supports.

The dispersion of active component was decided by the acidity of support surface and interaction between the active component and support. Ruckenstein and Wang [25] reported that the catalyst was more difficult to reduce if the metal–support interaction was stronger, but after reduction the metallic particles had stronger anti-sintering ability, resulting that the catalysts showed higher activity and stability. In our research, for the $Co/Ce_{0.33}Zr_{0.67}O_2$, the best dispersion of Co_3O_4 was acquired from the acidity of ZrO_2 and the strongest synergy effect of cobalt–support interaction (as shown in TPR measurements).

Fig. 4 showed the XRD patterns of catalysts after the reaction. Compared with the fresh catalysts, the reflection peaks of CeO_2 became sharper over the Co/CeO_2, suggesting that Co/CeO_2 had poor thermal stability. In addition, it could be seen that the reflection peaks of CeO_2 appeared on the XRD pattern of $Co/Ce_{0.33}Zr_{0.67}O_2$, and $Co/Ce_{0.6}Zr_{0.4}O_2$ still presented the reflection peaks of solid solution. Kambolis et al. [26] showed that the formation of cubic structure is expected for ceria content up to 50 mol% CeO_2, while for higher zirconia content the structure is

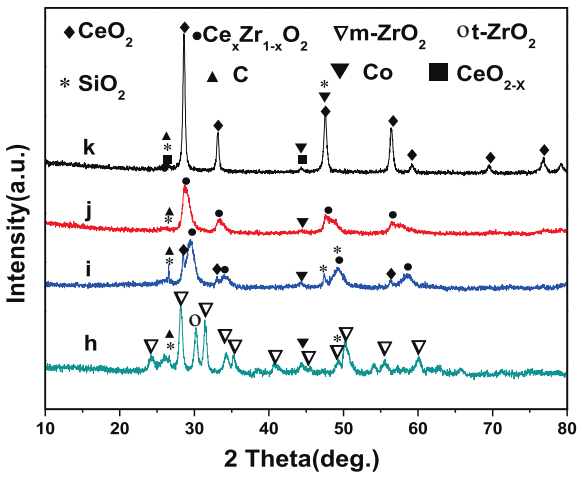

Fig. 4. XRD patterns of the catalysts after the reaction: (h) Co/ZrO_2; (i) $Co/Ce_{0.33}Zr_{0.67}O_2$; (j) $Co/Ce_{0.6}Zr_{0.4}O_2$; (k) Co/CeO_2.

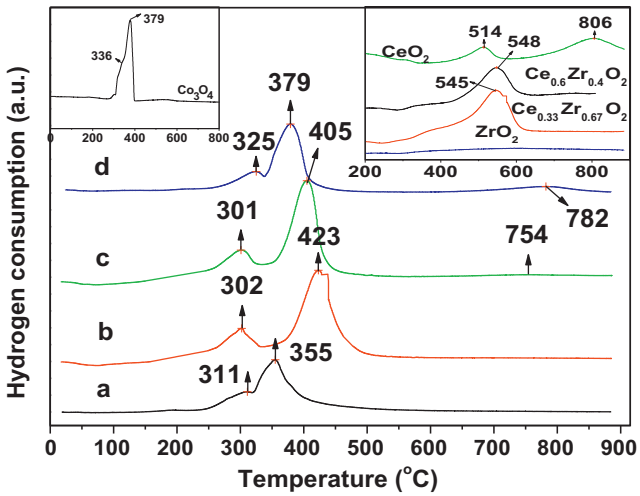

Fig. 5. H_2-TPR profiles of the Co_3O_4, supports and catalysts: (a) Co/ZrO_2; (b) $Co/Ce_{0.33}Zr_{0.67}O_2$; (c) $Co/Ce_{0.6}Zr_{0.4}O_2$; (d) Co/CeO_2.

tetragonal t' type or distorted tetragonal phase t'' type. Liu et al. [27] reported the $Pd/Ce_xZr_{1-x}O_2$ catalysts for methanol decomposition, and $Pd/Ce_{0.8}Zr_{0.2}O_2$ showed good stability in the reaction. It indicated that $Co/Ce_{0.6}Zr_{0.4}O_2$ retained the cubic fluorite structure after the reaction and had good thermal resistance because of higher CeO_2 content. Moreover, the reflection peaks of C, CeO_{2-x}, Co and SiO_2 also could be observed on the XRD patterns after the reaction. Carbon came from the carbon deposition in the reaction and SiO_2 was the quartz sand for dilution.

3.3. TPR measurements

Fig. 5 showed the H_2-TPR profiles of Co_3O_4, supports and catalysts, and the data of hydrogen consumption were listed in Table 3. Pure Co_3O_4 had two reductive peaks at about 336 °C and 379 °C, corresponding to the reduction of Co_3O_4 to CoO and CoO to Co respectively [8]. For CeO_2, the low temperature peak at 514 °C was ascribed to the reduction of surface oxygen, and the high temperature peak at 806 °C was the reduction of bulk lattice oxygen [28]. The $Ce_xZr_{1-x}O_2$ solid solution only had one reduction peak, respectively appeared at 545 °C for $Ce_{0.33}Zr_{0.67}O_2$ and 548 °C for $Ce_{0.6}Zr_{0.4}O_2$, which were attributed to the reduction of surface oxygen and bulk oxygen. Compared with CeO_2, the reduction of bulk oxygen shifted to lower temperature, suggesting that the replacement of Zr^{4+} ions in the lattice of CeO_2 promoted the reduction of bulk oxygen in the $Ce_xZr_{1-x}O_2$ solid solution, and it was accordant with the report of Wu et al. [28]. For ZrO_2, no obvious reduction peak was observed in the H_2-TPR profile.

For $Co/Ce_xZr_{1-x}O_2$ catalysts, the first step reductive peak of Co_3O_4 shifted to lower temperature and the second step reductive peak of Co_3O_4 shifted to higher temperature comparable to pure Co_3O_4. The order of CoO to Co reductive temperature was $Co/ZrO_2 < Co/CeO_2 < Co/Ce_{0.6}Zr_{0.4}O_2 < Co/Ce_{0.33}Zr_{0.67}O_2$, thus the order of cobalt–support synergy effect was $Co/Ce_{0.33}Zr_{0.67}O_2 > Co/Ce_{0.6}Zr_{0.4}O_2 > Co/CeO_2 > Co/ZrO_2$.

As shown in Table 3, the hydrogen consumption of $Co/Ce_xZr_{1-x}O_2$ catalysts markedly increased at the location of peaks I and II compared with Co/ZrO_2 and Co/CeO_2, indicating that the hydrogen consumption of $Co/Ce_xZr_{1-x}O_2$ catalysts included not only the reduction of Co_3O_4 but also the reduction of surface oxygen and bulk oxygen. It was obvious that the amount of hydrogen consumption increased with the increase of zirconium content for $Co/Ce_xZr_{1-x}O_2$ catalysts, which further confirmed that the reduction improvement of bulk oxygen was from the

Table 3
Reduction temperature and hydrogen consumption over the Co_3O_4 and catalysts.

Sample	Peak I		Peak II		Peak III		Total H_2 consumption (μmol g_{cat}^{-1})
	Temperature (°C)	H_2 consumption (%)[a]	Temperature (°C)	H_2 consumption (%)[a]	Temperature (°C)	H_2 consumption (%)[a]	
Co_3O_4	336	1101(20%)	379	4345(80%)	–	–	5446
Co/ZrO_2	311	1305(21%)	355	4956(79%)	–	–	8116
$Co/Ce_{0.33}Zr_{0.67}O_2$	302	4100(24%)	423	13012(76%)	–	–	17112
$Co/Ce_{0.6}Zr_{0.4}O_2$	301	3508(25%)	405	10508(75%)	–	–	14016
Co/CeO_2	325	2192(26%)	379	5193(61%)	782	1073(13%)	8548

[a] Relative proportion of hydrogen consumption.

structural distortion. From Table 1, the lattice parameters of cubic fluorite-type phase in the $Ce_xZr_{1-x}O_2$ were less than that of CeO_2, which led to a smaller cell volume. As mentioned by Wu et al. [28], the decrease of cell volume were favorable for the formation of defects and migration of bulk oxygen. Thus, the $Co/Ce_xZr_{1-x}O_2$ catalysts had better redox properties compared with Co/ZrO_2 and Co/CeO_2, which was helpful for improving catalytic activity and stability in the CO_2/CH_4 reforming reaction. In addition, for CeO_2, the reduction peaks I and II at 325 °C and 379 °C also included the reduction of surface oxygen except the reduction of cobalt oxides, and the reduction peak III at 782 °C was attributed to the reduction of bulk lattice oxygen [29].

3.4. Textural property analysis

Table 1 showed the textural property of supports and catalysts. The BET surface area of $Ce_xZr_{1-x}O_2$ was much higher than that of ZrO_2 and CeO_2. The BET surface area, pore diameter and pore volume of the catalysts decreased on different extent after loading cobalt, indicating that one part of cobalt oxides entered the pore path of supports, also another part of oxides dispersed on the surface of supports and jammed some pore path [30]. Among the catalysts, the $Co/Ce_{0.33}Zr_{0.67}O_2$ possessed the highest BET surface area, which was favorable for the dispersion of cobalt oxides. The Co/CeO_2 had the lowest BET surface area and its BET surface area and pore volume respectively decreased by 60.44% and 64.16% compared with CeO_2, suggesting that the porosity of CeO_2 was damaged during calcination process when loading cobalt. Therefore, the dispersion of cobalt oxides was the highest for $Co/Ce_{0.33}Zr_{0.67}O_2$ among the catalysts. This was consistent with the results of XRD measurements. From Table 1, the optimization order of BET surface area and pore volume was $Co/Ce_{0.33}Zr_{0.67}O_2 > Co/Ce_{0.6}Zr_{0.4}O_2 > Co/ZrO_2 > Co/CeO_2$.

Fig. 6 showed N_2 adsorption–desorption isotherms of the catalysts. According to five kinds of isotherms from BDDT pore model, they belonged to IV-type isotherms, corresponding to typical mesoporous solids. The pore structure was related to the shape of hysteresis loop on the adsorption–desorption isotherm. The hysteresis loop of Co/CeO_2 and $Co/Ce_xZr_{1-x}O_2$ was H2 loop, a characteristic of porous materials with wide pore diameter. The hysteresis loop of Co/ZrO_2 was H3 loop, and its adsorption capacity increased monotonously with pressure increase compared to the Co/CeO_2 and $Co/Ce_xZr_{1-x}O_2$. Fig. 7 showed BJH pore size distribution curves of the catalysts. It could be seen that they presented double pore distribution. The most probable peaks of the Co/CeO_2 and $Co/Ce_{0.6}Zr_{0.4}O_2$ appeared at 24 Å and 123 Å. The pore size distribution curve of $Co/Ce_{0.33}Zr_{0.67}O_2$ was similar to that of Co/CeO_2, and the most probable peaks appeared at 20 Å and 123 Å. For Co/ZrO_2, the pore diameter of bigger pores was wider than that of other three samples thus its adsorption–desorption isotherms were more steep.

From Figs. 6 and 7, the adsorption–desorption isotherms and the pore size distribution curves of $Co/Ce_xZr_{1-x}O_2$ were similar with those of Co/CeO_2, indicating that the mesoporous structure of $Co/Ce_xZr_{1-x}O_2$ was similar to that of Co/CeO_2. In addition, the most probable peak of small pore over the $Co/Ce_{0.33}Zr_{0.67}O_2$ shifted to smaller pore width compared to the $Co/Ce_{0.6}Zr_{0.4}O_2$. Moreover, the most probable peak of small pore over the Co/CeO_2 increased, suggesting that the amount of small pore increased.

In addition, the textural property of the spent catalysts also was showed in Table 1. It could be seen that the BET surface area of the catalysts decreased after the reaction, but the $Co/Ce_xZr_{1-x}O_2$ catalysts still maintained higher BET surface area comparable to ZrO_2 and CeO_2 after the reaction.

3.5. Catalytic performance

Fig. 8 showed the catalytic performance of Co/CeO_2, $Co/Ce_xZr_{1-x}O_2$ and Co/ZrO_2 catalysts with reaction temperature. It was clear that the activity of catalysts enhanced with

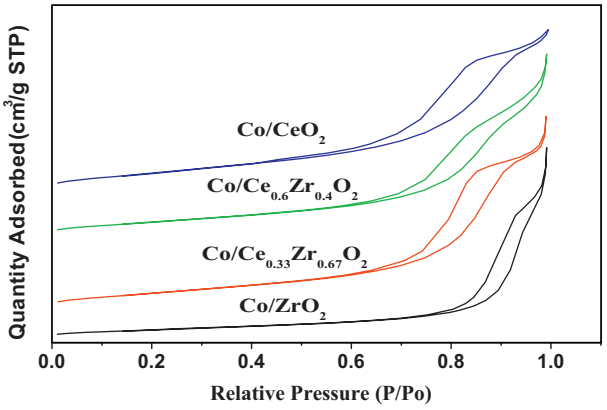

Fig. 6. N_2 adsorption–desorption isotherms of the catalysts.

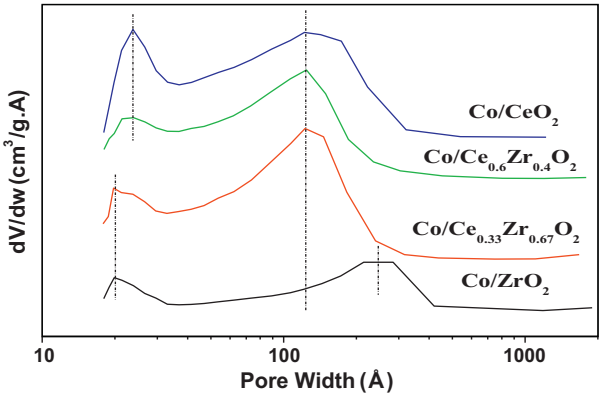

Fig. 7. Pore size distribution curves of the catalysts.

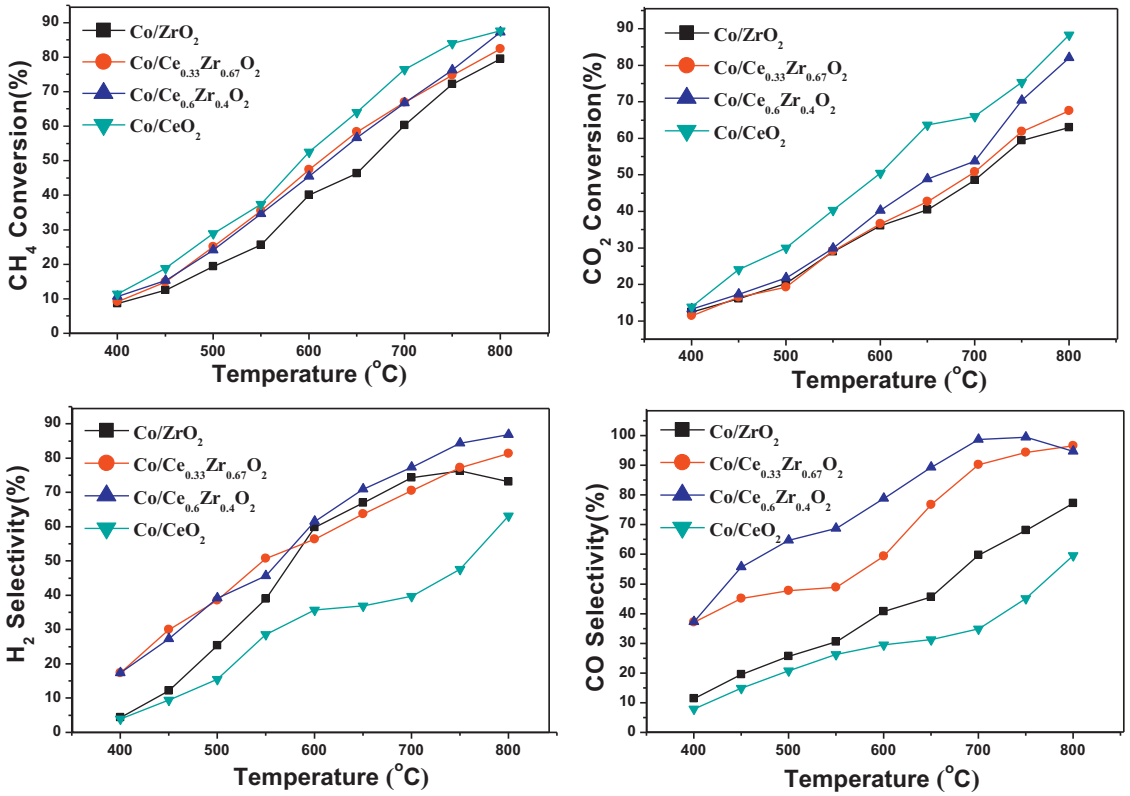

Fig. 8. CH_4 and CO_2 conversion as well as H_2 and CO selectivity over the catalysts with reaction temperature (CH_4/CO_2 = 1:1, T = 400–800 °C, GHSV = 8000 ml g_{cat}^{-1} h^{-1}, P = atmospheric pressure, 0.05 g catalyst).

the increase of reaction temperature because CO_2 reforming of methane was a strong endothermic reaction [28]. Among the catalysts, CH_4 and CO_2 conversions over the Co/CeO_2 were the highest, which was closely associated with the property of CeO_2 and the mechanism of CH_4/CO_2 reforming reaction. As shown in the NH_3-TPD analysis, CeO_2 was an alkali oxide. The alkalescence of CeO_2 support was favorable for adsorption and activation of CO_2 [26], then CO_2 was converted into CO. On the other hand, the lattice oxygen species on the surface of CeO_2 could oxidize CH_4 to CO and H_2. CeO_2 underwent a redox process via the mobility of lattice oxygen.

Similarly, the $Co/Ce_xZr_{1-x}O_2$ catalysts also showed better catalytic activity compared with Co/ZrO_2, which was attributed to good dispersion of the active species and redox properties of the $Ce_xZr_{1-x}O_2$ supports, as mentioned in the XRD and TPR measurements. Montoya et al. [22] reported that a significant increase in conversion was observed over the Ni/ZrO_2 catalyst when ceria was added into the catalyst, and they thought that CH_4 and CO_2 conversions increased with the increase of CeO_2 content. In this work, the activity of $Co/Ce_{0.6}Zr_{0.4}O_2$ was better than that of $Co/Ce_{0.33}Zr_{0.67}O_2$, and it was consistent with the above report. The low activity of Co/ZrO_2 resulted from the strongest acidity of support surface and the weak reducibility of support. In general, the activity of the samples was closely related with the acidity, dispersion and reducibility.

Moreover, H_2 and CO selectivity of the $Co/Ce_xZr_{1-x}O_2$ were better than those of Co/ZrO_2 and Co/CeO_2, especially for $Co/Ce_{0.6}Zr_{0.4}O_2$. In this reaction system, a sequence of elementary reactions had been proposed during CH_4/CO_2 reforming. They were shown as follows:

$$CH_4 + CO_2 \rightarrow 2CO + 2H_2 \quad (1)$$

$$CO_2 + H_2 \rightarrow H_2O + CO \quad (2)$$

$$CH_4 \rightarrow C + 2H_2 \quad (3)$$

$$CO + H_2 \rightarrow H_2O + C \quad (4)$$

$$2CO \rightarrow CO_2 + C \quad (5)$$

The reaction (1) was a strong endothermic reaction, and its equilibrium constant increased with the increase of reaction temperature, leading to the increase of catalytic activity. The reactions (2) and (3) were moderate endothermic reactions, thus the equilibrium constants also increased with the increase of reaction temperature. The reactions (4) and (5) were exothermic reactions and thermodynamically unfavorable at high temperature [4]. In this work, the reaction temperature was controlled from 400 °C to 800 °C. Zhang et al. [4] reported the variation of equilibrium constants of the above reactions. It was obvious that the low temperature before 650 °C was favorable for reactions 4 and 5, and the reactions 1, 2 and 3 began after 650 °C. The high selectivity of the $Co/Ce_xZr_{1-x}O_2$ was possible because the $Co/Ce_xZr_{1-x}O_2$ catalysts were more favorable for catalyzing the main reaction (reaction 1) than for promoting the side reactions (reactions (2) and (3)). In addition, Fig. 9 showed that the H_2/CO ratio of reaction product was close to one over the catalysts at 800 °C. The low H_2/CO ratio was preferentially used for the production of liquid hydrocarbons in the Fischer–Tropsch synthesis [5,6]. The H_2/CO ratio before 700 °C exceeded one just due to the influence of reactions (4) and (5). The ratio decreased when the reactions (1)–(3) began after 650 °C. Considering as a whole, the catalytic performance of $Co/Ce_{0.6}Zr_{0.4}O_2$ was the best among the catalysts, which was attributed to the alkalescence of support surface, better dispersion of active species, better textural property and reducibility.

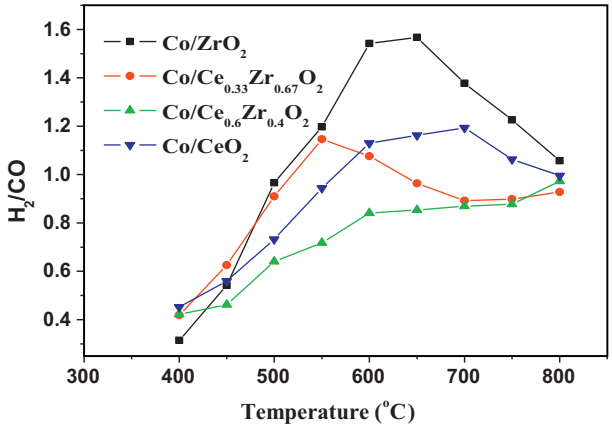

Fig. 9. H_2/CO ratio over the catalysts with reaction temperature (CH_4/CO_2 = 1:1, T = 400–800 °C, GHSV = 8000 ml g_{cat}^{-1} h^{-1}, P = atmospheric pressure, 0.05 g catalyst).

3.6. TEM analysis

Fig. 10 showed the TEM images of the fresh Co/ZrO_2 and $Co/Ce_{0.6}Zr_{0.4}O_2$ catalysts. Figs. 11 and 12 showed the TEM images of Co/ZrO_2 and $Co/Ce_{0.6}Zr_{0.4}O_2$ catalysts after reaction, respectively. For Co/ZrO_2, cobalt oxides (about 15–25 nm) dispersed on the supports of ZrO_2 (about 20 nm). The carbon filaments were observed over the Co/ZrO_2 catalyst after reaction (Fig. 11a), which were graphitic with the usual constant spacing between layer and layer (Fig. 11b). The metallic cobalt particles at the end of the carbon filaments were characteristic of pear form, which was consistent with the report about nickel catalysts [22]. As shown in Fig. 11c, the partial of carbon filaments contained cobalt particles shed from the surface of Co/ZrO_2 catalyst.

For $Co/Ce_{0.6}Zr_{0.4}O_2$ catalyst, the particle size of $Ce_{0.6}Zr_{0.4}O_2$ support was about 10 nm (Fig. 10). After reaction, the carbon filaments with graphitic structure were formed on the cobalt particles (Fig. 12b and c), and the diameters of carbon filaments were different. It was not obvious that the sizes of carbon filaments were closely related with the cobalt particle sizes, which was inconsistent the report of Montoya et al. [22]. As shown in Fig. 12, the carbon filaments easily formed on the bigger cobalt particles while the smaller cobalt particles was still exposed on the catalyst surface as the reaction active components because the reaction of eliminating carbon easily occurred on the smaller cobalt particles. As mentioned in the textural property analysis, $Co/Ce_xZr_{1-x}O_2$ still maintained higher BET surface area comparable to ZrO_2 and CeO_2 after the reaction. The high surface BET area of $Co/Ce_xZr_{1-x}O_2$ was favorable for cobalt dispersion on the support and could inhibit carbon formation on the catalysts.

By comparing the TEM images of the fresh and spent catalysts of Co/ZrO_2 with those of $Co/Ce_{0.6}Zr_{0.4}O_2$, it was clear that the conglomeration and carbon deposition were severe for the Co/ZrO_2

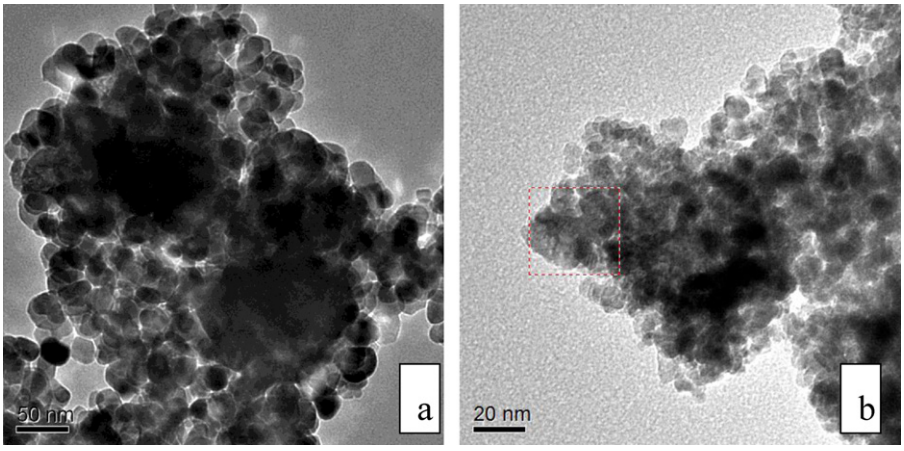

Fig. 10. TEM images of the catalysts before reaction: (a) Co/ZrO_2; (b) $Co/Ce_{0.6}Zr_{0.4}O_2$.

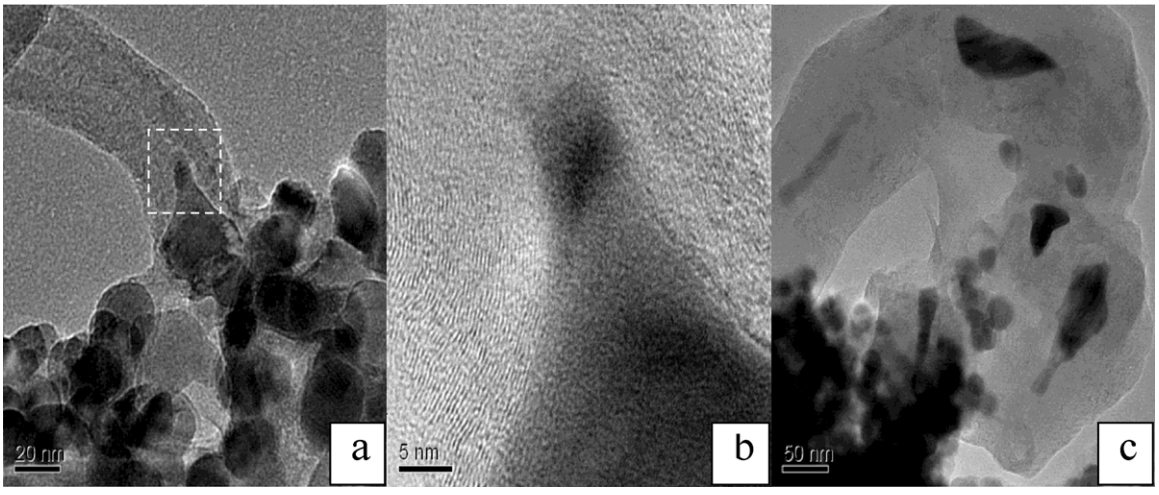

Fig. 11. TEM images of the Co/ZrO_2 catalyst after reaction (a and c); HRTEM images of the Co/ZrO_2 catalyst after reaction (b).

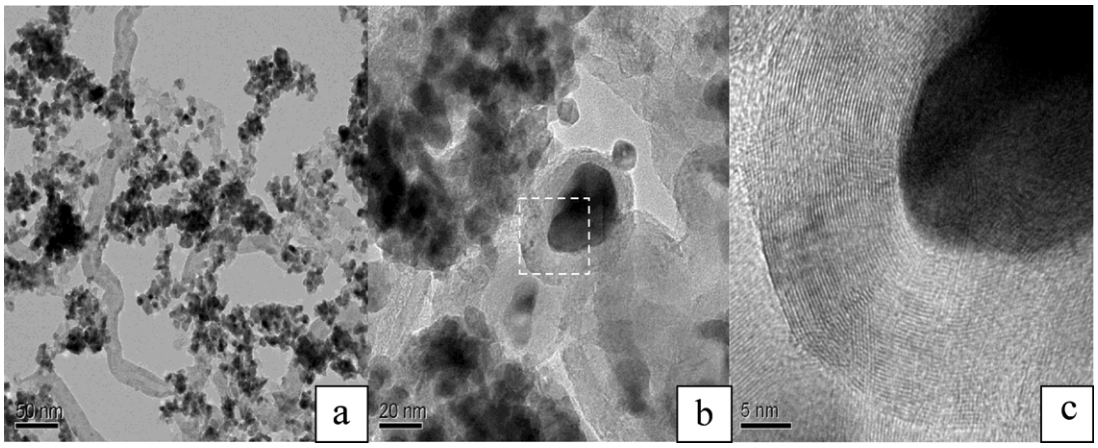

Fig. 12. TEM images of the $Co/Ce_{0.6}Zr_{0.4}O_2$ catalyst after reaction (a and b); HRTEM images of the $Co/Ce_{0.6}Zr_{0.4}O_2$ catalyst after reaction (c).

catalyst, but the $Co/Ce_{0.6}Zr_{0.4}O_2$ catalyst did not congregate and only small quantity of carbon was formed after reaction. It was the reason why the catalytic performance of two catalysts was significantly different. As discussed in Sections of 3.2 and 3.4, the ZrO_2 support had low BET surface area and was unfavorable for the acidic CO_2 adsorption thus the metallic cobalt over the Co/ZrO_2 catalyst easily congregated in the reaction. But for the $Co/Ce_{0.6}Zr_{0.4}O_2$, the increase content of alkaline CeO_2 was beneficial to adsorb and activate CO_2, accelerate the rate of carbon consumption and reduce carbon deposition. Moreover, the $Ce_{0.6}Zr_{0.4}O_2$ catalyst had high BET surface area and kept cubic fluorite structure after the reaction, which was verified by the analyses of XRD and textural property, therefore, the $Co/Ce_{0.6}Zr_{0.4}O_2$ could effectively prevented metallic cobalt from congregating in the reaction.

3.7. Coke deposition analysis

Fig. 13 showed TG–DSC curves of the spent catalysts under air atmosphere. The data of carbon deposition were listed in Table 4. Among the catalysts, the deposition carbon amount of $Co/Ce_xZr_{1-x}O_2$ was lower than that of Co/ZrO_2 and Co/CeO_2. The weight loss peaks appeared on the TG curves of the catalysts corresponded to the DSC exothermic peaks of deposition carbon combustion over the catalysts in the air. As seen in Fig. 13, there were three kinds of deposition carbon on the catalysts according to the temperature of elimination carbon, named as α carbon (low temperature), β carbon (medium temperature) and γ carbon (high temperature). Only one-type carbon (β carbon) existed in the Co/ZrO_2 catalyst, and it could be removed at about 500 °C. For Co/CeO_2, there were two kinds of deposition carbon after the reaction, including β carbon and γ carbon. β carbon could be eliminated at about 500 °C and the higher temperature (610 °C) was requested to remove γ carbon. For $Co/Ce_xZr_{1-x}O_2$, α carbon and β carbon existed in the catalysts after the reaction, indicating that carbon was easy to eliminate from the $Co/Ce_xZr_{1-x}O_2$ catalysts at low and medium temperature, which was closely related with their reducibility.

For $Co/Ce_{0.6}Zr_{0.4}O_2$, the ratio of α carbon to β carbon was 2.03, indicating that the deposition carbon over the $Co/Ce_{0.6}Zr_{0.4}O_2$ catalyst mainly existed in the form of low-temperature carbon, therefore, it showed the best catalytic performance and the lowest deposition carbon amount. For $Ce_{0.33}Zr_{0.67}O_2$, the ratio of α carbon/β carbon was 0.38 and the deposition carbon amount was 30.91%, therefore, its catalytic performance was weaker than that of $Co/Ce_{0.6}Zr_{0.4}O_2$ in despite of its higher BET surface area and better dispersion of cobalt oxides.

Table 4
The carbon deposition on the catalysts after reaction.

Sample	Coke deposition (wt%)	α carbon/β carbon
Co/ZrO_2	42.13	–
$Co/Ce_{0.33}Zr_{0.67}O_2$	30.91	0.38
$Co/Ce_{0.6}Zr_{0.4}O_2$	23.29	2.03
Co/CeO_2	33.95	–

Reaction conditions: $CH_4/CO_2 = 1:1$, $T = 400–800$ °C, GHSV = 8000 ml g_{cat}^{-1} h^{-1}, P = atmospheric pressure, 0.05 g catalyst.

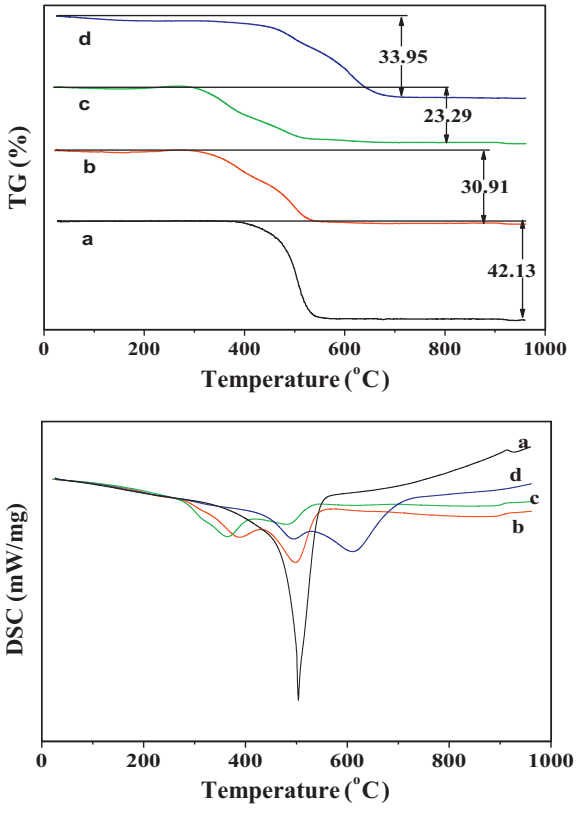

Fig. 13. TG–DSC curves of the spent catalysts under air atmosphere: (a) Co/ZrO_2; (b) $Co/Ce_{0.33}Zr_{0.67}O_2$; (c) $Co/Ce_{0.6}Zr_{0.4}O_2$; (d) Co/CeO_2.

4. Conclusions

The $Co/Ce_xZr_{1-x}O_2$ catalysts were prepared by the impregnation method. XRD measurements showed that the $Co/Ce_xZr_{1-x}O_2$ catalysts had a good dispersion of Co_3O_4 crystallites on the cubic fluorite $Ce_xZr_{1-x}O_2$ supports and the $Co/Ce_{0.6}Zr_{0.4}O_2$ retained the cubic fluorite structure after the reaction. TPR experiments indicated that the $Co/Ce_xZr_{1-x}O_2$ catalysts had good redox properties, which was helpful for improving catalytic activity and stability in the CO_2/CH_4 reforming reaction. Textural property analyses presented that the $Co/Ce_xZr_{1-x}O_2$ catalysts had high BET surface area. The performance tests showed that the catalytic performance of $Ce_{0.6}Zr_{0.4}O_2$ was the best among the as-prepared catalysts, which was attributed to the alkalescence of support surface, better dispersion of active species, better textural property and reducibility. TEM and coke deposition analyses indicated that the $Co/Ce_{0.6}Zr_{0.4}O_2$ catalyst didn't congregate and only small quantity of carbon was formed after reaction, and the deposition carbon over the $Co/Ce_{0.6}Zr_{0.4}O_2$ catalyst mainly existed in the form of low-temperature carbon.

Acknowledgments

The authors would like to acknowledge the National Natural Science Foundation of China (grant no. 21061008) and the Natural Science Foundation of Inner Mongolia (grant no. 2010ZD01, 2010BS0202). Thank editor and reviewers for giving us the valuable suggestions.

References

[1] M.S. Moreno, F. Wang, M. Malac, T. Kasama, C.E. Gigola, I. Costilla, M.D. Sánchez, Journal of Applied Physics 105 (2009) 083531–083536.
[2] M.H. Amin, K. Mantri, J. Newnham, J. Tardio, S.K. Bhargava, Applied Catalysis B: Environmental 119–120 (2012) 217–226.
[3] C.K. Shi, P. Zhang, Applied Catalysis B: Environmental 115–116 (2012) 190–200.
[4] J.G. Zhang, H. Wang, A.K. Dalai, Journal of Catalysis 249 (2007) 300–310.
[5] D.P. Liu, L. Raymond, B. Armando, Applied Catalysis A: General 358 (2009) 110–118.
[6] S. Damyanova, B. Pawelec, K. Arishtirova, M.V.M. Huerta, J.L.G. Fierro, Applied Catalysis B: Environmental 89 (2009) 149–159.
[7] E. Ruckenstein, H.Y. Wang, Journal of Catalysis 205 (2002) 289–293.
[8] K. Takanabe, K. Nagaoka, K. Nariai, K. Aika, Journal of Catalysis 230 (2005) 75–85.
[9] Z.C. Liu, J. Zhou, K. Cao, W.M. Yang, H.X. Gao, Y.D. Wang, H.X. Li, Applied Catalysis B: Environmental 125 (2012) 324–330.
[10] S.M. Stagg, E. Romeo, C. Padro, D.E. Resasco, Journal of Catalysis 178 (1998) 137–145.
[11] F.B. Noronha, E.C. Fendley, R.R. Soares, W.E. Alvarez, D.E. Resasco, Chemical Engineering Journal 82 (2001) 21–31.
[12] T. Hayakawa, S. Suzuki, J. Nakamura, T. Uchijima, S. Hamakawa, K. Suzuki, T. Shishido, K. Takehira, Applied Catalysis A: General 183 (1999) 273–285.
[13] N. Wang, W. Chu, L.Q. Huang, T. Zhang, Journal of Natural Gas Chemistry 19 (2010) 117–122.
[14] J.R. Anderson, M. Boudart, Catalysis: Science and Technology, Springer, New York, 1982.
[15] M. Masai, H. Kado, A. Miyake, S. Nishiyama, S. Tsuruya, Studies in Surface Science and Catalysis 36 (1988) 67–71.
[16] M. Ji, M.J. Zhou, Y.L. Bi, K.J. Zhen, Journal of Molecular Catalysis (China) 11 (1997) 6–12.
[17] Y.H. Hu, Catalysis Today 148 (2009) 206–211.
[18] H.S. Roh, H.S. Potdar, K.W. Jun, Catalysis Today 93–95 (2004) 39–44.
[19] J.X. Chen, Q.Y. Wu, J.X. Zhang, J.Y. Zhang, Fuel 87 (2008) 2901–2907.
[20] H.S. Roh, H.S. Potdar, K.W. Jun, J.W. Kim, Y.S. Oh, Applied Catalysis A: General 276 (2004) 231–239.
[21] A. Shotipruk, S. Assabumrungrat, P. Pavasant, N. Laosiripojana, Chemical Engineering Science 64 (2009) 459–466.
[22] J.A. Montoya, E. Romero-Pascual, C. Gimon, P.D. Angel, Catalysis Today 63 (2000) 71–85.
[23] J.X. Chen, C.C. Yao, Y.Q. Zhao, P.H. Jia, International Journal of Hydrogen Energy 35 (2010) 1630–1642.
[24] A. Martinez, C. Lopez, F. Marquez, I. Diaz, Journal of Catalysis 220 (2003) 486–499.
[25] E. Ruckenstein, H.Y. Wang, Applied Catalysis A: General 204 (2000) 257–263.
[26] A. Kambolis, H. Matralis, A. Trovarelli, C. Papadopoulou, Applied Catalysis A: General 377 (2010) 16–26.
[27] Y.Y. Liu, T. Hayakawa, T. Ishii, M. Kumagai, H. Yasuda, K. Suzuki, S. Hamakawa, K. Murata, Applied Catalysis A: General 210 (2001) 301–314.
[28] Q.Y. Wu, J.X. Chen, J.Y. Zhang, Fuel Processing Technology 89 (2008) 993–999.
[29] H.C. Yao, Y.F.Y. Yao, Journal of Catalysis 86 (1984) 254–265.
[30] H.Q. Su, S.H. Zeng, H. Dong, Y. Du, Y.L. Zhang, R.S. Hu, Applied Clay Science 46 (2009) 325–329.